Journal of Materials Chemistry C

ROYAL SOCIETY OF CHEMISTRY

PAPER

View Article Online
View Journal | View Issue

Cite this: J. Mater. Chem. C, 2024, 12, 16367

Design of alkali lead oxybromides with a strong second-harmonic generation response and large birefringence†

Jialin Zeng,[ab] Shuangcheng Li,[a] Yahui Zhu,[a] Zilong Geng,[ad] Yiting Luo,[ab] Ruibiao Fu *[ad] and Zuju Ma*[c]

Received 11th July 2024,
Accepted 29th August 2024

DOI: 10.1039/d4tc02947j

rsc.li/materials-c

Nonlinear optical (NLO) crystals are of importance in modern lasers, high-precision micromachining, ultrahigh resolution photolithography and advanced scientific equipment. Herein, we have rationally obtained two new lead oxybromides, $A_3[Pb_2Br_5(OOC(CH_2)_3COO)]$ (A = Rb, Cs), with a strong second-harmonic generation (SHG) response and large birefringence. Two neighboring highly distorted $[PbBr_4O_2]$ polyhedrons with high polarizability and anisotropic polarization are bridged by the flexible glutarate group and one Br^- anion to form a large $[Pb_2Br_7(OOC(CH_2)_3COO)]$ group. Interestingly, the large $[Pb_2Br_7(OOC(CH_2)_3COO)]$ groups are induced by Rb^+/Cs^+ cations into an oriented alignment, leading to the effective superimposition of their microscopic second-order susceptibility and the enhancement of optical anisotropy. Notably, $Rb_3[Pb_2Br_5(OOC(CH_2)_3COO)]$ exhibits good comprehensive NLO performance, including a strong phase-matching SHG response of 3.1 × KDP, a large birefringence of 0.207@546 nm, a wide high transparency window, easy growth of large single crystals, as well as good thermal stability up to 240 °C under an air atmosphere. On the basis of their crystal structures and theoretical calculations, their strong SHG responses mainly stem from the highly distorted $[PbBr_4O_2]$ polyhedron. This research provides an effective strategy for the design and pursuit of high-performance NLO crystals in the future.

Introduction

Nonlinear optical (NLO) crystals are an important class of photoelectric functional materials which have the frequency conversion ability to generate new coherent light, and are thus widely applied in modern lasers, high-precision micromachining, ultrahigh resolution photolithography, medical treatment, laser nuclear fusion and advanced scientific equipment.[1–9] Therefore, the development of practical NLO crystals has attracted great research interest in the past few decades, resulting in the development of some commercialized NLO crystals, like $AgGaS_2$ (AGS),[10] $AgGaSe_2$ (AGSe),[11] $ZnGeP_2$ (ZGP),[12] $KTiOPO_4$ (KTP),[13] $LiNbO_3$ (LN),[14] KH_2PO_4 (KDP),[15] β-BaB_2O_4 (BBO),[16] LiB_3O_5 (LBO)[17] and $KBe_2BO_3F_2$ (KBBF).[18] However, these NLO crystals have respective inherent drawbacks, such as the relatively weak second-harmonic generation (SHG) response of KDP. Although LBO is a popular NLO crystal with a short cut-off edge of 160 nm, it cannot be used in the deep-ultraviolet region due to its small birefringence.[19] Driven by the increasing demand for laser technology, it is urgent to explore new NLO crystals with excellent comprehensive performance, especially those with strong SHG response and large birefringence. In view of this, several lead oxyhalides displaying intriguing NLO properties, such as $Pb_{13}O_6Cl_4Br_{10}$, $Pb_{13}O_6Cl_7Br_7$, $Pb_{13}O_6Cl_9Br_5$, $Pb_{18}O_8Cl_{15}I_5$, Pb_2BO_3X (X = Cl, Br, and I) and $Pb_{17}O_8Cl_{18}$, have aroused our research interest.[20–26] In particular, Pb_2BO_3I is composed of a lead-oxyiodide $[PbO_3I_2]$ polyhedron which is shared by well-arranged $[BO_3]$ triangular plane units *via* oxygen atoms.[26] Pb_2BO_3I exhibits a remarkable SHG response of 10 × KDP for the synergistic effect of the $[PbO_3I_2]$ polyhedrons and the coplanar $[BO_3]$ SHG-active units. Inspired by these results, we have attempted to modify the $[PbX_6]$ (X = Br, I) octahedrons in lead halide perovskites through the substitution of partial halide anions with carboxylate oxygen atoms, giving rise to several strong NLO crystals.[27–30]

[a] State Key Laboratory of Structural Chemistry, Fujian Institute of Research on the Structure of Matter, Chinese Academy of Sciences, Fuzhou, Fujian 350002, P. R. China. E-mail: furb@fjirsm.ac.cn
[b] College of Chemistry and Materials Science, Fujian Normal University, Fuzhou, Fujian 350007, P. R. China
[c] School of Environmental and Materials Engineering, Yantai University, Yantai, 264005, P. R. China. E-mail: zjma@outlook.com
[d] University of Chinese Academy of Sciences, Beijing 100049, China

† Electronic supplementary information (ESI) available: Computational details, crystal data, and additional tables and figures. CCDC 2357098 and 2357099. For ESI and crystallographic data in CIF or other electronic format see DOI: https://doi.org/10.1039/d4tc02947j

Nevertheless, it is still difficult to effectively synthesize lead oxyhalide NLO crystals because nearly 79% of lead oxyhalides containing distorted $[PbO_nX_m]$ (X = Cl, Br, I) polyhedrons in the Inorganic Crystal Structure Database crystallize in centrosymmetric structures, resulting in them being SHG-inert in nature. To address this challenge, the strategy of introducing both the flexible glutarate group and alkali metal cations with a large ionic radius into lead halides has been put forward to rationally explore high-performance NLO crystals based on the following considerations: (1) the carboxylate oxygen atoms and halide anions could simultaneously coordinate with the Pb(II) atom, leading to a twisted lead-centered coordination polyhedron; (2) the flexible glutarate group can adopt suitable configurations to bridge the distorted lead-oxyhalide polyhedrons to form large anionic groups; (3) alkali metal cations with a large ionic radius like Rb^+ and Cs^+ cations can be incorporated into the structure to contact with large anionic groups through coulombic interactions. This can weaken the dipole–dipole interactions among large anionic groups and thus facilitate the formation of noncentrosymmetric (NCS) structures that is a prerequisite for the generation of SHG response.[31,32] In this paper, two strong lead oxybromide NLO crystals with a large birefringence, $A_3[Pb_2Br_5(OOC(CH_2)_3COO)]$ (A = Rb, Cs), have been rationally obtained. It is interesting that the large $[Pb_2Br_7(OOC(CH_2)_3COO)]$ groups consisting of two highly distorted $[PbBr_4O_2]$ coordination polyhedrons with high polarizability and anisotropic polarization are in an oriented alignment. Notably, $Rb_3[Pb_2Br_5(OOC(CH_2)_3COO)]$ not only exhibits good comprehensive NLO performance, including a strong phase-matching SHG response of 3.1 × KDP, a large birefringence of 0.207@546 nm, a wide high transparency window, and easy growth of large single crystals, but is also thermally stable up to 240 °C under an air atmosphere.

Experimental

Reagents

Lead oxide (PbO, 99%, Aladdin), glutaric acid ($C_5H_8O_4$, 99%, Aladdin), rubidium bromide (RbBr, 99.8%, Anhui Senrise), cesium bromide (CsBr, 99.9%, Macklin) and absolute ethanol (EtOH, 99.7%, Sinopharm) were purchased from commercial sources and used as received without further purification.

Synthesis

Large crystals of $A_3[Pb_2Br_5(OOC(CH_2)_3COO)]$ (A = Rb, Cs) were synthesized by a mixed-solvothermal method (Fig. S1 and S2, ESI†). Glutaric acid (0.264 g, 2.00 mmol), PbO (0.223 g, 1.00 mmol), RbBr (0.496 g, 3.00 mmol)/CsBr (0.638 g, 3.00 mmol), 2 mL EtOH and 1 mL H_2O were added into a 25 mL Teflon-lined stainless steel autoclave and heated to 130 °C for 3 days, and then gradually cooled to room temperature at a rate of 0.83 °C h^{-1}. Based on PbO, the yields were 47 and 18% for $Rb_3[Pb_2Br_5(OOC(CH_2)_3COO)]$ and $Cs_3[Pb_2Br_5(OOC(CH_2)_3COO)]$, respectively. Their phase purities were validated by the fact that their experimental powder X-ray diffraction (PXRD) patterns are in good agreement with those simulated from the respective single-crystal X-ray diffraction data (Fig. S3 and S4, ESI†). Energy dispersive X-ray spectroscopy (EDS) spectra reveal the coexistence of Rb/Cs, Pb, Br, O and C elements (Fig. S5 and S6, ESI†). The atomic ratios of both Rb : Pb : Br (7.8 : 5.5 : 13.5) and Cs : Pb : Br (8.4 : 5.7 : 13.7) accord with the theoretical value of 1.5 : 1 : 2.5 based on single-crystal X-ray diffraction analysis. In the IR spectra, the two absorption bands at 1525/1527 and 1410/1411 cm^{-1} are attributed to the stretching vibrations of the carboxylate group (Fig. S7 and S8, ESI†). Meanwhile, two peaks at 1454/1452 and 750/748 cm^{-1} belong to the scissoring and rocking vibrations of the $-CH_2$ group, respectively. Hence, their IR spectra support the presence of the glutarate group. Analysis calculated (anal. calcd) for $Rb_3[Pb_2Br_5(OOC(CH_2)_3COO)]$: C 5.00%, H 0.50%. Found: C 4.90%, H 0.83%. And anal. calcd for $Cs_3[Pb_2Br_5(OOC(CH_2)_3COO)]$: C 4.47%, H 0.45%. Found: C 4.43%, H 0.93%. Elemental analysis of C and H matches well with their theoretical values.

Single-crystal X-ray diffraction

Single-crystal X-ray diffraction data were collected on a Rigaku XtaLAB Synergy diffractometer equipped with a graphite-monochromated Cu Kα radiation source (λ(Cu-Kα) = 1.54184 Å). The CrysAlisPro 1.171.41.98a program was used to perform data reduction. Their structures were solved by the direct method with the aid of the SHELXT program and further refined using the SHELXL full-matrix least-squares program.[33,34] And no higher symmetries were suggested after checking their structures with the PLATON.[35] The crystallographic data are summarized in Tables S1 and S2 (ESI†). The atomic coordinates, equivalent isotropic displacement parameters, bond valence sum (BVS), anisotropic displacement parameters, and selected bond lengths and angles are listed in Tables S3–S8 (ESI†) (CCDC 2357098 for $K_3[Pb_2Br_5(OOC(CH_2)_3COO)]$ and 2357099 for $Cs_3[Pb_2Br_5(OOC(CH_2)_3COO)]$†).

Powder X-ray diffraction

PXRD measurements were carried out at room temperature on a Rigaku Miniflex 600 diffractometer equipped with a Cu Kα radiation source (λ = 1.540598 Å). Variable-temperature PXRD patterns were recorded on a Rigaku MiniFlex II diffractometer with Cu Kα radiation (λ = 1.540598 Å). All data were obtained in the 2θ range of 5–55° with a step size of 0.02°.

Thermogravimetric analysis (TGA)

TGA was performed on a NETZSCH STA 449F3 thermal analysis instrument by using an Al_2O_3 crucible as a reference. Under a flow of nitrogen gas, the temperature was increased from 30 to 800 °C at a heating rate of 10 °C min^{-1}.

Energy dispersive X-ray spectroscopy and elemental analyses

Microprobe elemental analyses were performed by using a field emission scanning electron microscope (FESEM, JSM6700F) with an EDS (Oxford INCA). C and H analyses were carried out using a Vario EL III elemental analyzer.

Optical spectroscopy

According to the attenuated total reflectance method, the IR spectrum was recorded on a VERTEX70 FT-IR spectrometer

instrument at room temperature. The crystal sample was tightly fitted to the total reflection crystal and then the data were collected in the range of 400 to 4000 cm^{-1}. The UV-vis-NIR diffuse reflectance spectrum was recorded on a PerkinElmer Lambda 950 ultraviolet/visible/near-infrared spectrophotometer with $BaSO_4$ as the standard reference in the wavelength range of 190–2500 nm. The reflection spectrum was converted into the absorption spectrum based on the Kubelka–Munk function: $\alpha/S = F(R) = (1 - R)^2/2R$ (where S is the scattering coefficient, α is the absorption coefficient, and R is the reflectance).[36,37]

Second-harmonic generation and laser damage threshold (LDT) measurements

SHG measurements were performed on a pulsed Q-switched Nd:$Y_3Al_5O_{12}$ (YAG) solid-state laser by a modified Kurtz–Perry method at a wavelength of 1064 nm and room temperature.[38] Crystalline samples and microcrystalline KDP as the references were ground and then sieved using standard sieves with a pore size of 355, 212, 150, 109, 75, 53, 45 and 25 μm. Then, samples with progressively increasing particle size ranges of 25–45, 45–53, 53–75, 75–109, 109–150, 150–212 and 212–355 μm were obtained. $Rb_3[Pb_2Br_5(OOC(CH_2)_3COO)]$ and $Cs_3[Pb_2Br_5(OOC(CH_2)_3COO)]$ with particle size ranges of 212–270 and 250–380 μm, respectively, were employed to test their LDTs under a 1064 nm laser source (10 ns, 1 Hz and 0.2 cm^2 for the laser spot area). The laser energy was gradually enhanced until the color of the sample changed.

Computational details

In order to study the origin of NLO performance, density functional theory (DFT) calculations have been carried out by using the Vienna *ab initio* simulation package (VASP)[39,40] with the Perdew–Burke–Ernzerhof (PBE)[41] exchange correlation functional. The projector augmented wave (PAW)[42] potentials have been used to treat the ion–electron interactions. A Γ-centered 3 × 5 × 5 (for $Rb_3[Pb_2Br_5(OOC(CH_2)_3COO)]$) or 5 × 3 × 5 (for $Cs_3[Pb_2Br_5(OOC(CH_2)_3COO)]$) Monkhorst–Pack grid for the Brillouin zone sampling[43] and a cutoff energy of 500 eV for the plane wave expansion were employed to obtain convergent lattice parameters and self-consistent energies. In the calculation of the static $\chi^{(2)}$ coefficients, we adopt the length–gauge formalism derived by Aversa and Sipe[44] and modified by Rashkeev *et al.*,[45] which has been proved to be successful in calculating the second order susceptibility for semiconductors and insulators.[46–48] The dynamic SHG coefficient is calculated based on the formula developed by Aversa and Sipe[44] and Rashkeev *et al.*[45]

Results and discussion

Crystal structures

Crystals of $A_3[Pb_2Br_5(OOC(CH_2)_3COO)]$ (A = Rb, Cs) were successfully obtained by the mixed-solvothermal method (Fig. S1 and S2, ESI†). The purity of the products was fully verified by PXRD, EDS, IR and elemental analyses. It is interesting that a single crystal of $Rb_3[Pb_2Br_5(OOC(CH_2)_3COO)]$ can grow easily to a large size of 5 × 1 × 0.5 mm^3, implying its feasible crystal growth. Single-crystal X-ray diffraction reveals that $Rb_3[Pb_2Br_5(OOC(CH_2)_3COO)]$ and $Cs_3[Pb_2Br_5(OOC(CH_2)_3COO)]$ crystallize in the NCS polar space groups of *Imm*2 and *Amm*2, respectively. Owing to their similar structures, $Rb_3[Pb_2Br_5(OOC(CH_2)_3COO)]$ is selected as a representative to describe their detailed structures. Firstly, the Pb(II) atom is coordinated by four Br^- anions into a $[PbBr_4]$ group (Fig. 1a), in which the Pb1–Br1 and Pb1–Br3 bonds slightly lean upward, while the Pb1–Br2 and Pb1–Br4 bonds tilt downward. As expected, the Pb(II) atom is also chelated by the terminal carboxylate group of the glutarate ligand from one side of the $[PbBr_4]$ group (Fig. 1a and b). The Pb–O bond distances are 2.523(9) and 2.570(11) Å, which are obviously shorter than those of Pb–Br bonds. Meanwhile, the O1–Pb1–O2 bond angle is only 51.0(3)°, obviously deviating from the ideal 90° for a regular octahedron. Secondly, the electron localization function (ELF) demonstrates that there is a strong localized distribution of electrons around the Pb(II) atom (Fig. 1c). This implies that the lone pair on the Pb(II) atom is stereochemically active and is located on the other side of the $[PbBr_4]$ group. Finally, the electronegativity of oxygen is larger than that of bromine. The above factors contribute to the great distortion of the $[PbBr_4O_2]$ coordination polyhedron.

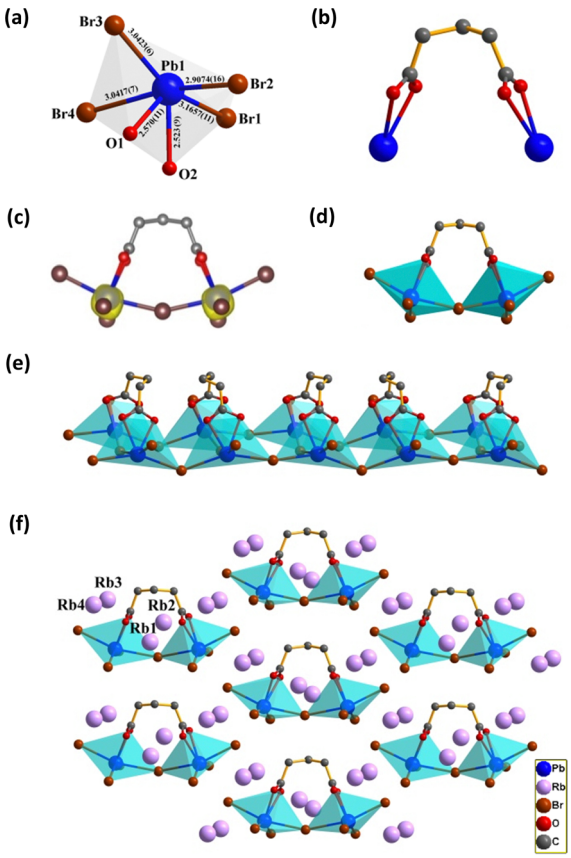

Fig. 1 (a) The coordination environment of the Pb(II) atom. (b) The coordination mode of the glutarate group. (c) The ELF plot with an isovalue of 0.93 shown with the yellow beige lobes. (d) The large $[Pb_2Br_7(OOC(CH_2)_3COO)]$ group. (e) The double $[Pb_2Br_5(OOC(CH_2)_3COO)]$ chain. (f) The structure of $Rb_3[Pb_2Br_5(OOC(CH_2)_3COO)]$. The blue-green polyhedron represents $[PbBr_4O_2]$.

Correspondingly, the distorted $[PbBr_4O_2]$ coordination polyhedron has a large dipole moment of 7.61 D (Table S9, ESI†).[46] Thus, the highly distorted $[PbBr_4O_2]$ polyhedron with high polarizability is conducive to the generation of a strong SHG response.

On the other hand, the two terminal carboxylate groups of the glutarate ligand bend toward same direction to chelate two Pb(II) atoms. As a result, two neighbouring distorted $[PbBr_4O_2]$ polyhedrons are combined by the glutarate group and one Br^- anion, giving rise to a large $[Pb_2Br_7(OOC(CH_2)_3COO)]$ group (Fig. 1d). This configuration is in favor of the superposition of the polarizations from the highly distorted $[PbBr_4O_2]$ polyhedron. The large $[Pb_2Br_7(OOC(CH_2)_3COO)]$ groups are further connected by $Br1^-$ and $Br3^-$ anions into a double $[Pb_2Br_5(OOC(CH_2)_3COO)]$ chain (Fig. 1e). Both $Rb1^+$ and $Rb2^+$ cations are in the polar $[RbBr_4O_4]$ unit with four Br^- anions located on one side and four oxygen atoms occupying the opposite side (Fig. S9, ESI†). Thus, these Rb^+ cations are embedded into the double $[Pb_2Br_5(OOC(CH_2)_3COO)]$ chain not only to compensate the charge, but also to induce the large $[Pb_2Br_7(OOC(CH_2)_3COO)]$ groups into an oriented arrangement (Fig. 1e and Fig. S10, ESI†). Meanwhile, the void spaces among the double $[Pb_2Br_5(OOC(CH_2)_3COO)]$ chains are filled with $Rb3^+$ and $Rb4^+$ cations (Fig. 1f). Thus, the double $[Pb_2Br_5(OOC(CH_2)_3COO)]$ chains are separated by $Rb3^+$ and $Rb4^+$ cations to avoid dipole–dipole interactions.[31,32] Since both $Rb3^+$ and $Rb4^+$ cations are also in a distorted $[RbBr_6O_2]$ unit (Fig. S9, ESI†), the double $[Pb_2Br_5(OOC(CH_2)_3COO)]$ chains are further induced by $Rb3^+$ and $Rb4^+$ cations to align along the uniform orientation with the lone pairs of the Pb(II) atom on the same side. Remarkably, the large $[Pb_2Br_7(OOC(CH_2)_3COO)]$ groups are in an oriented arrangement which is beneficial to the superposition of their polarization to generate a strong SHG response and large birefringence. Furthermore, the BVS values for Rb/Cs, Pb, Br and O atoms have been calculated with reasonable values of 0.79–1.13/0.89–1.22, 1.90–2.02, −1.03 to −0.74 and −2.15 to −1.89, which are in accordance with their expected valences of +1, +2, −1 and −2, respectively.[49] This result further supports the reliability of their structures.

Stability

TGA curves recorded under nitrogen gas flow indicate that a slight weight loss was observed up to 315 and 290 °C for $Rb_3[Pb_2Br_5(OOC(CH_2)_3COO)]$ and $Cs_3[Pb_2Br_5(OOC(CH_2)_3COO)]$ (Fig. S11 and S12, ESI†), respectively. And $Rb_3[Pb_2Br_5(OOC(CH_2)_3COO)]$ was selected as a representative to further confirm their thermal stability by variable-temperature PXRD. At 240 °C, experimental PXRD patterns agree well with those simulated from single-crystal X-ray diffraction data (Fig. S13, ESI†), suggesting that $Rb_3[Pb_2Br_5(OOC(CH_2)_3COO)]$ is thermally stable up to 240 °C under an air atmosphere. Notably, $Rb_3[Pb_2Br_5(OOC(CH_2)_3COO)]$ exhibits higher thermal stability compared with the popular KDP NLO crystal which has a phase transition temperature of 187 °C.[50] Additionally, the LDTs of $Rb_3[Pb_2Br_5(OOC(CH_2)_3COO)]$ and $Cs_3[Pb_2Br_5(OOC(CH_2)_3COO)]$ were measured to be 41 and 44 MW cm^{-2}, respectively. Therefore, good stability will favor their practical application.

NLO properties

Their UV-vis-NIR diffuse reflectance spectra are shown in Fig. S14 and S15 (ESI†). Especially, $Rb_3[Pb_2Br_5(OOC(CH_2)_3COO)]$ displays high reflectance from 427 to 2500 nm, covering most of the visible light and near infrared region. Their absorption bands extend into the UV region with peaks around 330 nm. Based on the Kubelka–Munk function, $Rb_3[Pb_2Br_5(OOC(CH_2)_3COO)]$ and $Cs_3[Pb_2Br_5(OOC(CH_2)_3COO)]$ possess optical band gaps of 3.33 and 3.32 eV, respectively.[36,37] These values are close to their respective calculated band gaps using the DFT method (Fig. S16 and S17, ESI†).[39–41] According to linear optical calculations, both $A_3[Pb_2Br_5(OOC(CH_2)_3COO)]$ (A = Rb, Cs) are optically negative uniaxial crystals. They show gradual increases in refractive indices along with the enhancement of the photon energy and display strong optical anisotropy (Fig. 2a and Fig. S18, ESI†). And $Rb_3[Pb_2Br_5(OOC(CH_2)_3COO)]$ and $Cs_3[Pb_2Br_5(OOC(CH_2)_3COO)]$ possess large calculated birefringence values of 0.20@1064 nm and 0.15@1064 nm (Fig. 2b and Fig. S19, ESI†), respectively, which are large enough for the phase-matching during the SHG process. In addition, the birefringence of $Rb_3[Pb_2Br_5(OOC(CH_2)_3COO)]$ has also been measured on a ZEISS Axio A1 polarizing microscope.[51] For a small unpolished single crystal with a thickness of 89.79 μm, complete extinction is achieved at a delay value of 18.4 μm (Fig. 2c and d and Fig. S20, ESI†), corresponding to a birefringence of 0.207 at a wavelength of 546 nm. It is worth noting that the observed birefringence is not only greater than those of the popular NLO crystals like KTP (0.10@530 nm) and BBO (0.12@532 nm), but also superior to those of commercial birefringent crystals, such as α-BBO (0.122@532 nm) and $CaCO_3$ (0.174@533 nm). Since the birefringence is closely related to the polarizability anisotropy of structural units and their spatial arrangement, the source of their large birefringence is studied by calculating the polarizability anisotropy of

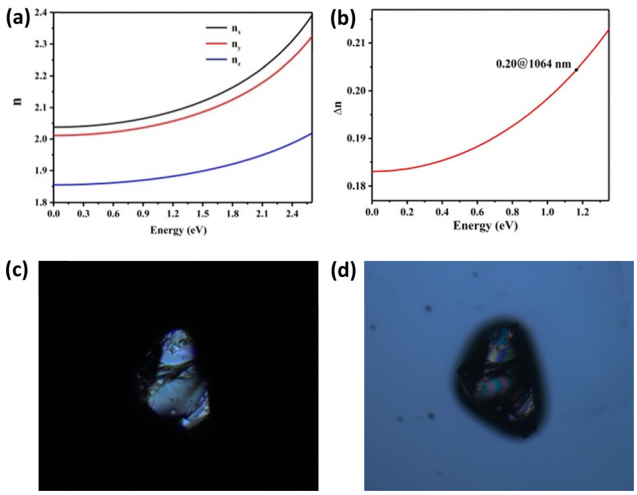

Fig. 2 (a) Optical refractive indices along the principal axes and (b) the calculated birefringence *versus* photon energy for $Rb_3[Pb_2Br_5(OOC(CH_2)_3COO)]$. (c) The original crystal for the measurement of the birefringence under a polarizing microscope. (d) The crystal achieving complete extinction.

the distorted $[PbBr_4O_2]$ polyhedron and the $[C_5H_6O_4]$ group (Tables S9 and S10, ESI†). The polarizability anisotropy of the distorted $[PbBr_4O_2]$ polyhedron obviously surpasses that of the $[C_5H_6O_4]$ group. In addition, there are strongly localized electrons around the Pb(II) atoms (Fig. 1c), which are intrinsically correlated with the 6s lone pairs. Moreover, the $[Pb_2Br_7(OOC(CH_2)_3COO)]$ groups are in an oriented alignment with the 6s lone pairs on the same side, giving rise to obvious optical anisotropy. Therefore, the great polarizability anisotropy of the distorted $[PbBr_4O_2]$ polyhedron and the oriented arrangement of the $[Pb_2Br_7(OOC(CH_2)_3COO)]$ groups are responsible for their large birefringence.

Since $A_3[Pb_2Br_5(OOC(CH_2)_3COO)]$ (A = Rb, Cs) crystallize in NCS polar space groups, the Kurtz–Perry method was employed to measure their SHG responses under 1064 nm laser irradiation on a Q-switched Nd:YAG laser.[38] As shown in Fig. 3a and b, $A_3[Pb_2Br_5(OOC(CH_2)_3COO)]$ (A = Rb, Cs) exhibit good phase-matching behavior at 1064 nm because their SHG intensities increase steadily along with increasing particle sizes. This agrees with the fact that they possess large birefringence to satisfy phase-matching. Remarkably, $A_3[Pb_2Br_5(OOC(CH_2)_3COO)]$ (A = Rb, Cs) display strong SHG responses of 3.1 × KDP within the particle size range of 212–355 μm (Fig. 3c and d). Their SHG responses are stronger than those of $Pb_3(SeO_3)Br_4$ (1 × KDP) and $Pb_2NbO_2(SeO_3)_2Br$ (1.4 × KDP).[52,53] Furthermore, a very strong SHG response can also be observed on a single crystal of $Rb_3[Pb_2Br_5(OOC(CH_2)_3COO)]$ with a size of 4 × 1 × 1 mm^3. More importantly, $Rb_3[Pb_2Br_5(OOC(CH_2)_3COO)]$ crystals can still display a strong SHG response after being heated at 200 °C for one hour under an air atmosphere. This is in agreement with the high thermal stability of $Rb_3[Pb_2Br_5(OOC(CH_2)_3COO)]$. Owing to their strong phase-matching SHG response, large birefringence, wide high transparency window and good stability, $A_3[Pb_2Br_5(OOC(CH_2)_3COO)]$ (A = Rb, Cs) serve as new promising NLO crystals.

Theoretical studies

The polarity is usually considered to be the source of SHG response.[54] Therefore, we have calculated the local dipole moments of the distorted $[PbBr_4O_2]$ polyhedron and the $[OOC(CH_2)_3COO]$ group to disclose the origin of their strong SHG response (Tables S9 and S10, ESI†).[46] Both the *x*- and *y*-components of their polarization are completely cancelled out. In contrast, the *z*-component of the polarization from the distorted $[PbBr_4O_2]$ polyhedron is effectively superimposed (Fig. 4a). Although the polarization is weakened by the $[OOC(CH_2)_3COO]$ group because the *z*-component of the polarization from the $[OOC(CH_2)_3COO]$ group is on the opposite direction, both $Rb_3[Pb_2Br_5(OOC(CH_2)_3COO)]$ and $Cs_3[Pb_2Br_5(OOC(CH_2)_3COO)]$ still have large net polarization values of −21.12 and 18.48 D in each respective unit cell. This is in agreement with the oriented arrangement of the large $[Pb_2Br_7(OOC(CH_2)_3COO)]$ groups. On the other hand, the ELF map reveals strongly localized electrons around the Pb(II) atoms, corresponding to the 6s lone pairs (Fig. 1c and 4b). The lobule-shaped electrons point to the same side and will induce large polarization under the external field

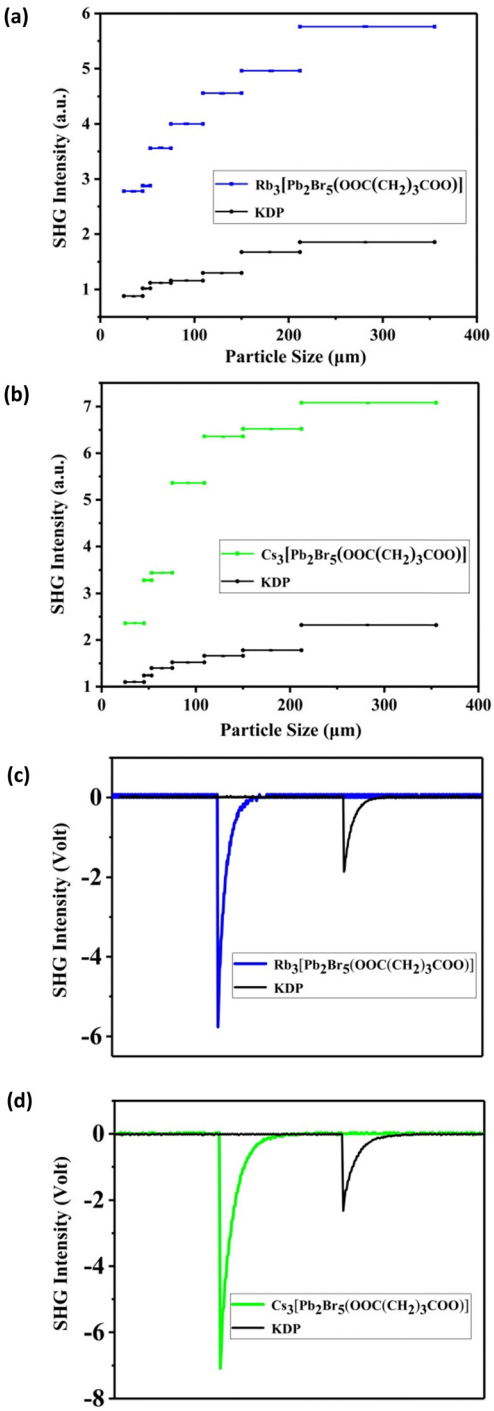

Fig. 3 SHG intensities of (a) $Rb_3[Pb_2Br_5(OOC(CH_2)_3COO)]$, (b) $Cs_3[Pb_2Br_5(OOC(CH_2)_3COO)]$, and KDP under different particle sizes. SHG intensities of (c) $Rb_3[Pb_2Br_5(OOC(CH_2)_3COO)]$ and (d) $Cs_3[Pb_2Br_5(OOC(CH_2)_3COO)]$ and KDP within the particle size range of 212–355 μm.

perturbation, which is beneficial for the generation of a strong SHG response. Overall, the distorted $[PbBr_4O_2]$ polyhedron makes the main contribution to their strong SHG responses.

To perform a deep investigation into the microscopic mechanism of their NLO properties, systematic theoretical calculations were further carried out on the basis of the DFT

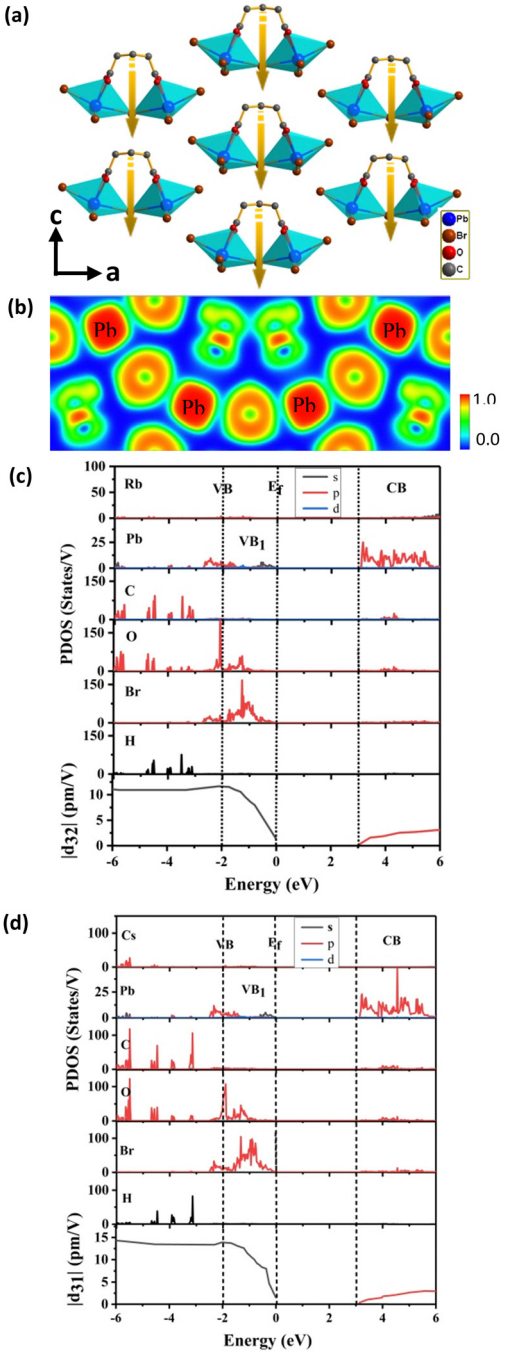

Fig. 4 (a) The oriented arrangement of the double $[Pb_2Br_5(OOC(CH_2)_3COO)]$ chains in $Rb_3[Pb_2Br_5(OOC(CH_2)_3COO)]$. Blue–green polyhedron: $[PbBr_4O_2]$. The yellow arrow denotes the direction of the net dipole moment for the double $[Pb_2Br_5(OOC(CH_2)_3COO)]$ chain. (b) The ELF of the *ac* plane for $Rb_3[Pb_2Br_5(OOC(CH_2)_3COO)]$, in which a value less than 0.5 indicates the electrons to be delocalized, while a value between 0.5 and 1.0 in regions denotes bonding and non-bonding localized electrons. PDOS and cutoff-energy-dependent SHG coefficient of (c) $Rb_3[Pb_2Br_5(OOC(CH_2)_3COO)]$ and (d) $Cs_3[Pb_2Br_5(OOC(CH_2)_3COO)]$.

method.[39–41] The calculated band gaps of $Rb_3[Pb_2Br_5(OOC(CH_2)_3COO)]$ and $Cs_3[Pb_2Br_5(OOC(CH_2)_3COO)]$ are 3.08 and 3.14 eV (Fig. S16 and S17, ESI†), respectively, which are close to their experimental values. According to the NCS space groups of *Imm*2 and *Amm*2, both of them possess three distinct nonzero independent SHG coefficients under the restriction of Kleinman symmetry (Fig. S21 and S22, ESI†).[55] The static SHG coefficients of $|d_{31}|$, $|d_{32}|$ and $|d_{33}|$ are 0.504, 11.354 and 2.285 pm V^{-1} for $Rb_3[Pb_2Br_5(OOC(CH_2)_3COO)]$, and 13.695, 0.891 and 4.878 pm V^{-1} for $Cs_3[Pb_2Br_5(OOC(CH_2)_3COO)]$. It is well known that electronic transitions between the valence bands (VBs) and the conduction bands (CBs) close to the Fermi energy usually dominate the optical properties of a crystal.[56] Therefore, their electronic structures near the Fermi level (E_f, set at 0 eV) are studied in detail. The partial density of states (PDOS) of the constitutional atoms are shown in Fig. 4c and d. The VBs ranging from −6.0 to −3.0 eV depend on the O 2p, C 2p and H 1s orbitals. It can be clearly seen that the top region of VBs spanning from −3.0 to 0 eV is mainly occupied by O 2p and Br 4p electrons, which are hybridized with a small number of Pb 6s electrons, while in the bottom region of CBs, the dominant orbital contributions stem from Pb 6p, O 2p and C 2p states. On the other hand, Rb^+/Cs^+ orbitals are away from the Fermi energy and make little contributions to both the top of the VBs and the bottom of the CBs. Furthermore, the cutoff-energy-dependent SHG coefficients with the aid of the length-gauge formalism have also been calculated to clearly investigate the contribution of individual bands.[44,45] Notably, $|d_{32}|$ (for $Rb_3[Pb_2Br_5(OOC(CH_2)_3COO)]$) and $|d_{31}|$ (for $Cs_3[Pb_2Br_5(OOC(CH_2)_3COO)]$) SHG coefficients increase in magnitude in the VB1 region which is mainly constructed from Br 4p, O 2p and Pb 6s electrons. Meanwhile, these SHG coefficients are also enhanced steadily in the bottom region of CBs which originates predominantly from vacant Pb 6p states. To sum up, it is the distorted $[PbBr_4O_2]$ polyhedron that makes considerable contribution to their strong SHG responses. This is in agreement with the fact that the oriented arrangement of the large $[Pb_2Br_7(OOC(CH_2)_3COO)]$ groups is beneficial for the effective superimposition of the microscopic second-order susceptibility of the distorted $[PbBr_4O_2]$ polyhedrons.

Conclusions

In summary, new lead oxybromide NLO crystals with a strong SHG response and large birefringence, $A_3[Pb_2Br_5(OOC(CH_2)_3COO)]$ (A = Rb, Cs), have been rationally obtained under mild mixed-solvothermal conditions. Two neighboring highly distorted $[PbBr_4O_2]$ polyhedrons with high polarizability and anisotropic polarization are combined by the flexible glutarate group and one Br^- anion to form a large $[Pb_2Br_7(OOC(CH_2)_3COO)]$ group. It is interesting that the large $[Pb_2Br_7(OOC(CH_2)_3COO)]$ groups are induced by Rb^+/Cs^+ cations into an oriented alignment, giving rise to the effective superimposition of their microscopic second-order susceptibility and the enhancement of optical anisotropy. More importantly, $Rb_3[Pb_2Br_5(OOC(CH_2)_3COO)]$ not only exhibits good comprehensive NLO performance, including a strong phase-matching SHG response of 3.1 × KDP, a large birefringence of 0.207@546 nm, a wide high transparent window, and easy growth of large single crystals,

but is also thermally stable up to 240 °C under an air atmosphere. This research provides an effective strategy for the design and pursuit of high-performance NLO crystals in the future.

Author contributions

Jialin Zeng: synthesis, characterization and writing – original manuscript & editing. Ruibiao Fu: methodology, supervision, writing – review & editing. Zuju Ma: theoretical calculations. Shuangcheng Li, Yahui Zhu, Zilong Geng and Yiting Luo: discussion.

Data availability

The data supporting this article have been included as part of the ESI.†

Conflicts of interest

The authors declare no conflicts of interest.

Acknowledgements

This work was supported by the National Natural Science Foundation of China (22275184 and 22273081). We sincerely thank Bingxuan Li and Zujian Wang for the measurement of LDT and birefringence, respectively.

Notes and references

1 M. Mutailipu, J. Han, Z. Li, F. M. Li, J. J. Li, F. F. Zhang, X. F. Long, Z. H. Yang and S. L. Pan, Achieving the full-wavelength phase-matching for efficient nonlinear optical frequency conversion in $C(NH_2)_3BF_4$, *Nat. Photonics*, 2023, **17**, 694–701.

2 R. A. Li, Q. Q. Liu, X. Liu, Y. Q. Liu, X. X. Jiang, Z. S. Lin, F. Jia, L. Xiong, L. Chen and L. M. Wu, $Na_2Ba[Na_2Sn_2S_7]$: Structural tolerance factor-guided NLO performance improvement, *Angew. Chem., Int. Ed.*, 2023, **62**, e202218048.

3 L. Qi, X. X. Jiang, K. Duanmu, C. Wu, Z. S. Lin, Z. P. Huang, M. G. Humphrey and C. Zhang, Quadruple-bidentate nitrate-ligated $A_2Hg(NO_3)_4$ (A = K, Rb): Strong second-harmonic generation and sufficient birefringence, *Angew. Chem., Int. Ed.*, 2023, **62**, e202309365.

4 N. Savage, Ultraviolet lasers, *Nat. Photonics*, 2007, **1**, 83–85.

5 H. N. Liu, H. P. Wu, Z. G. Hu, J. Y. Wang, Y. C. Wu and H. W. Yu, $Cs_3[(BOP)_2(B_3O_7)_3]$: A deep-ultraviolet nonlinear optical crystal designed by optimizing matching of cation and anion groups, *J. Am. Chem. Soc.*, 2023, **145**, 12691–12700.

6 X. H. Dong, H. B. Huang, L. Huang, Y. Q. Zhou, B. B. Zhang, H. M. Zeng, Z. E. Lin and G. H. Zhou, Unearthing superior inorganic UV second-order nonlinear optical materials: A mineral-inspired method integrating first-principles high-throughput screening and crystal engineering, *Angew. Chem., Int. Ed.*, 2024, **63**, e202318976.

7 X. F. Wang, X. D. Leng, Y. Kuk, Q. Jing and K. M. Ok, Deep-ultraviolet transparent mixed metal sulfamates with enhanced nonlinear optical properties and birefringence, *Angew. Chem., Int. Ed.*, 2024, **63**, e202315434.

8 M. Mutailipu and S. L. Pan, Emergent deep-ultraviolet nonlinear optical candidates, *Angew. Chem., Int. Ed.*, 2020, **59**, 20302–20317.

9 X. Huang, S. H. Yang, X. H. Li, W. L. Liu and S. P. Guo, Eu2P2S6: The first rare-earth chalcogenophosphate exhibiting large second-harmonic generation response and high laserInduced damage threshold, *Angew. Chem., Int. Ed.*, 2022, **61**, e202206791.

10 A. O. Okorogu, S. B. Mirov, W. Lee, D. I. Crouthamel, N. Jenkins, A. Y. Dergachev, K. L. Vodopyanov and V. V. Badikov, Tunable middle infrared downconversion in GaSe and $AgGaS_2$, *Opt. Commun.*, 1998, **155**, 307–312.

11 G. D. Boyd, F. G. Storz, J. H. McFee and H. M. Kasper, Linear and nonlinear optical properties of some ternary selenides, *IEEE J. Quantum Electron.*, 1972, **8**, 900–908.

12 G. D. Boyd, Linear and nonlinear optical properties of $ZnGeP_2$ and CdSe, *Appl. Phys. Lett.*, 1971, **18**, 301–304.

13 J. D. Bierlein and H. Vanherzeele, Potassium titanyl phosphate: Properties and new applications, *J. Opt. Soc. Am. B*, 1989, **6**, 622–633.

14 G. D. Boyd, R. C. Miller, K. Nassau, W. L. Bond and A. Savage, $LiNbO_3$: An efficient phase matchable nonlinear optical material, *Appl. Phys. Lett.*, 1964, **5**, 234–236.

15 W. L. Smith, KDP and ADP transmission in the vacuum ultraviolet, *Appl. Opt.*, 1977, **5**, 1798.

16 L. Cheng, W. Bosenberg and C. Tang, Broadly tunable optical parametric oscillation in β-BaB_2O_4, *Appl. Phys. Lett.*, 1988, **53**, 175–177.

17 Y. Mori, I. Kuroda, S. Nakajima, T. Sasaki and S. Nakai, New nonlinear optical crystal: Cesium lithium borate, *Appl. Phys. Lett.*, 1995, **67**, 1818–1820.

18 C. T. Chen, G. L. Wang, X. Y. Wang and Z. Y. Xu, Deep-UV nonlinear optical crystal $KBe_2BO_3F_2$-discovery, growth, optical properties and applications, *Appl. Phys. B: Lasers Opt.*, 2009, **97**, 9–25.

19 T. T. Tran, H. W. Yu, J. M. Rondinelli, K. R. Poeppelmer and P. S. Halasyamani, Deep ultraviolet nonlinear optical materials, *Chem. Mater.*, 2016, **28**, 5238–5258.

20 X. L. Chen and K. M. Ok, Metal oxyhalides: An emerging family of nonlinear optical materials, *Chem. Sci.*, 2022, **13**, 3942–3956.

21 X. L. Chen, H. Jo and K. M. Ok, Lead mixed oxyhalides satisfying all fundamental requirements for high-performance mid-infrared nonlinear optical materials, *Angew. Chem., Int. Ed.*, 2020, **59**, 7514–7520.

22 X. L. Chen, Q. Jing and K. M. Ok, $Pb_{18}O_8Cl_{15}I_5$: A polar lead mixed oxyhalide with unprecedented architecture and excellent infrared nonlinear optical properties, *Angew. Chem., Int. Ed.*, 2020, **59**, 20323–20327.

23 G. H. Zou, C. S. Lin, H. Jo, G. Nam, T. S. You and K. M. Ok, Pb_2BO_3Cl: A tailor-made polar lead borate chloride with very strong second harmonic generation, *Angew. Chem., Int. Ed.*, 2016, **55**, 12078–12082.

24 M. Luo, Y. X. Song, F. Liang, N. Ye and Z. S. Lin, Pb_2BO_3Br: A novel nonlinear optical lead borate bromine with a KBBF-type structure exhibiting strong nonlinear optical response, *Inorg. Chem. Front.*, 2018, **5**, 916–921.

25 H. W. Yu, N. Z. Joocher, J. M. Rondinelli and P. S. Halasyamani, Pb_2BO_3I: A borate iodide with the largest second-harmonic generation (SHG) response in the $KBe_2BO_3F_2$ (KBBF) family of nonlinear optical (NLO) materials, *Angew. Chem., Int. Ed.*, 2018, **57**, 6100–6103.

26 H. Zhang, M. Zhang, S. L. Pan, X. Y. Dong, Z. H. Yang, X. L. Hou, Z. Wang, K. B. Chang and K. R. Poeppelmeier, Pb17O8Cl18: A promising IR nonlinear optical material with large laser damage threshold synthesized in an open system, *J. Am. Chem. Soc.*, 2015, **137**, 8360–8363.

27 Q. R. Shui, H. X. Tang, R. B. Fu, Y. B. Fang, Z. J. Ma and X. T. Wu, $Cs_3Pb_2(CH_3COO)_2X_5$ (X = I, Br): Halides with strong second-harmonic generation response induced by acetate groups, *Angew. Chem., Int. Ed.*, 2021, **60**, 2116–2119.

28 X. Y. Zhang, Z. Q. Zhou, W. X. Bao, H. X. Tang, R. B. Fu, Z. J. Ma and X. T. Wu, New lead-iodide formates with a strong second-harmonic generation response and suitable birefringence obtained by the substitution strategy, *Chem. Sci.*, 2023, **14**, 136–142.

29 Z. Q. Zhou, R. B. Fu, H. X. Tang, Z. J. Ma and X. T. Wu, An excellent lead oxyiodide with a strong second-harmonic generation response and a large birefringence induced by the oriented arrangement of highly distorted $[PbO_4I_2]$ polyhedral, *Inorg. Chem. Front.*, 2022, **9**, 4464–4469.

30 S. C. Li, Z. L. Geng, R. B. Fu, Z. J. Ma and X. T. Wu, A potassium lead 2-methylmalonate-iodide nonlinear optical crystal with strong second-harmonic generation response and large birefringence, *Scr. Mater.*, 2024, **239**, 115824.

31 S. R. Marder, J. W. Perry and W. P. Schaefer, Synthesis of organic salts with large second-order optical nonlinearities, *Science*, 1989, **245**, 626–628.

32 J. Lu, X. Liu, M. Zhao, X. B. Deng, K. X. Shi, Q. R. Wu, L. Chen and L. M. Wu, Discovery of NLO semiorganic $(C_5H_6ON)^+(H_2PO_4)^-$: Dipole moment modulation and superior synergy in solar-blind UV region, *J. Am. Chem. Soc.*, 2021, **143**, 3647–3654.

33 G. M. Sheldrick, Crystal structure refinement with SHELXL, *Acta Crystallogr., Sect. C: Struct. Chem.*, 2015, **71**, 3–8.

34 G. M. Sheldrick, SHELXT-integrated space-group and crystal-structure determination, *Acta Crystallogr., Sect. A: Found. Adv.*, 2015, **71**, 3–8.

35 A. L. Spek, Single-crystal structure validation with the program PLATON, *J. Appl. Crystallogr.*, 2003, **36**, 7–13.

36 P. Kubelka and F. Munk, An article on optics of paint layers, *Z. Tech. Phys.*, 1931, **12**, 259–274.

37 J. Tauc, Absorption edge and internal electric fields in amorphous semiconductors, *Mater. Res. Bull.*, 1970, **5**, 721–729.

38 S. Kurtz and T. Perry, A powder technique for the evaluation of nonlinear optical materials, *J. Appl. Phys.*, 1968, **39**, 3798–3813.

39 G. Kresse and J. Furthmüller, Efficient iterative schemes for ab initio total-energy calculations using a plane-wave basis set, *Phys. Rev. B: Condens. Matter Mater. Phys.*, 1996, **54**, 11169–11186.

40 G. Kresse and D. Joubert, From ultrasoft pseudopotentials to the projector augmented-wave method, *Phys. Rev. B: Condens. Matter Mater. Phys.*, 1999, **59**, 1758–1775.

41 J. P. Perdew, K. Burke and M. Ernzerhof, Generalized gradient approximation made simple, *Phys. Rev. Lett.*, 1996, **77**, 3865–3868.

42 P. E. Blochl, Projector augmented-wave method, *Phys. Rev. B: Condens. Matter Mater. Phys.*, 1994, **50**, 17953–17979.

43 H. J. Monkhorst and J. D. Pack, Special points for Brillouin-zone integrations, *Phys. Rev. B: Solid State*, 1976, **13**, 5188–5192.

44 C. Aversa and J. Sipe, Nonlinear optical susceptibilities of semiconductors: Results with a length-gauge analysis, *Phys. Rev. B: Condens. Matter Mater. Phys.*, 1995, **52**, 14636–14645.

45 S. N. Rashkeev, W. R. L. Lambrecht and B. Segall, Efficient ab initio method for the calculation of frequency-dependent second-order optical response in semiconductors, *Phys. Rev. B: Condens. Matter Mater. Phys.*, 1998, **57**, 3905–3919.

46 Z. Ma, J. Hu, R. Sa, Q. Li, Y. Zhang and K. Wu, Screening novel candidates for mid-IR nonlinear optical materials from I_3–V–VI_4 compounds, *J. Mater. Chem. C*, 2017, **5**, 1963–1972.

47 Z. Fang, J. Lin, R. Liu, P. Liu, Y. Li, X. Huang, K. Ding, L. Ning and Y. Zhang, Computational design of inorganic nonlinear optical crystals based on a genetic algorithm, *CrystEngComm*, 2014, **16**, 10569–10580.

48 Y. C. Yang, X. Liu, J. Lu, L. M. Wu and L. Chen, $[Ag(NH_3)_2]_2SO_4$: A strategy for the coordination of cationic moieties to design nonlinear optical materials, *Angew. Chem., Int. Ed.*, 2021, **60**, 21216–21220.

49 N. E. Brese and M. O'Keeffe, Bond-valence parameters for solids, *Acta Crystallogr., Sect. B: Struct. Sci.*, 1991, **47**, 192–197.

50 I. Piñeres, E. Ortiz, C. De la Hoz, J. Tróchez and C. León, On the nature of the KH_2PO_4 high-temperature transformation, *Ionics*, 2017, **23**, 1187–1195.

51 H. Y. Sha, Y. R. Shang, Z. J. Wang, R. B. Su, C. He, X. M. Yang and X. F. Long, A sharp improvement of sulfate's birefringence induced by the synergistic effect of heteroleptic and dimeric strategies, *Small*, 2023, 202309776.

52 X. X. Wang, X. X. Jiang, H. M. Liu, L. Yang, Z. S. Lin, Z. G. Hu, X. G. Meng, X. G. Chen and J. G. Qin, $Pb_3(SeO_3)Br_4$: A new nonlinear optical material with enhanced SHG response designed via an ion-substitution strategy, *Dalton Trans.*, 2018, **47**, 1911–1917.

53 H. K. Zhao, P. F. Gong, X. Y. Zhang, Z. S. Lin, Z. G. Hu and Y. C. Wu, $Pb_4(OH)_4(BrO_3)_3(NO_3)$: An example of SHG crystal in metal bromates containing π-conjugated planar triangle, *Inorg. Chem.*, 2016, **55**, 948–955.

54 H. Y. Chang, S. H. Kim, K. M. Ok and P. S. Halasyamani, Polar or nonpolar? A^+ cation polarity control in $A_2Ti(IO_3)_6$(A = Li, Na, K, Rb, Cs, Tl), *J. Am. Chem. Soc.*, 2009, **131**, 6865–6873.

55 D. A. Kleinman, Nonlinear dielectric polarization in optical media, *Phys. Rev.*, 1962, **126**, 1977–1979.

56 M. H. Lee, C. H. Yang and J. H. Jan, Band-resolved analysis of nonlinear optical properties of crystalline and molecular materials, *Phys. Rev. B: Condens. Matter Mater. Phys.*, 2004, **70**, 235110.

